ADVANCED OPTICAL MATERIALS
www.advopticalmat.de

Bidirectional Photoresponse in Perovskite-ZnO Heterostructure for Fully Optical-Controlled Artificial Synapse

Shuaipeng Ge, Fengchang Huang, Jiaqi He, Zhangsheng Xu, Zhenhua Sun, Xun Han, Chunfeng Wang, Long-Biao Huang, and Caofeng Pan**

Compared with electrical synapses, optoelectronic synapses exhibit great potential for ultrafast computing and wireless communication in neuromorphic hardware with advantages of low crosstalk, high bandwidth, and low power consumption. However, due to the unidirectional photoresponse in most of optoelectronic synapses, the related researches still focus on the electrical stimulation of inhibitory behaviors. Herein, a synaptic device based on perovskite–ZnO heterostructure is prepared with the characteristic of bidirectional photoresponse and can realize both the potentiation and depression by ultraviolet (UV) and green light stimuli, respectively. Consecutive UV and green light stimuli for potentiation and depression reveal the reliability and repeatability of the fully optical-controlled artificial synapse. A series of logic functions including "OR," "AND," "NOR," and "NAND" has also been demonstrated in a fully-optical pathway. This work not only offers an innovative architecture based on the perovskite single crystal and ZnO for fully optical-controlled artificial synapse, but also represents a step toward optical wireless neuromorphic systems.

1. Introduction

Physical separation of memory and central processing units in conventional von Neumann architecture leads to immense energy consumption and inherent speed limitations. Inspired by human neural system, communicating through synapses with the features of parallel distributed processing and integrated storage and computation, various neuromorphic devices including memristors and field-effect transistors have been employed to simulate synaptic functions to overcome the von Neumann bottleneck.[1–3] Synaptic plasticity such as long/short-term potentiation (LTP/STP), long/short-term depression (LTD/STD), and paired pulse facilitation/depression (PPF/PPD), have been mimicked by modulating device conductivity (i.e., synaptic weight). Among these synaptic devices, potentiation and depression are always triggered by electrical stimulation. As known the electronic technology suffers the problem of limited computing speed because of the bandwidth connection density trade-off.[4]

Fortunately, optoelectronic synapses with the light stimuli exhibit potential for ultrafast computing with advantages of the low crosstalk, high bandwidth, and low power consumption, also can be applied in optical wireless communication.[5,6] Herein, the optoelectronic synapses are operated with direct light illumination and the output is interpreted from the change of electrical conductance. It is different from the photonic devices that are mentioned in the photonic integrated circuits, in which the light is illuminated through a waveguide and output is denoted by the transmittance/absorbance of light in the waveguide.[7,8] However, most of reported optoelectronic devices only show positive photoresponse corresponding to the potentiation behavior of synapses. The achievement of depression behavior still depends on electrical stimulation due to the unidirectional photoresponse of devices. Therefore, a device with bidirectional photoresponse to emulate both excitatory and inhibitory behaviors for a fully optical-controlled artificial synapse is highly desired.

Recently, a few of fully optical-controlled artificial synapses have been reported, such as pyrenyl graphdiyne/graphene/PbS heterostructure,[5] Bi_2O_2Se/graphene hybrid structure,[6] ZnO/PbS hybrid heterostructure,[9] oxygen-deficient/oxygen-rich InGaZnO homojunction, and black phosphorus.[10–13] Both the excitatory and inhibitory synaptic behaviors of

S. Ge, Z. Sun, C. Wang, L.-B. Huang
Key Laboratory of Optoelectronic Devices and Systems of Ministry of Education and Guangdong Province
College of Physics and Optoelectronic Engineering
Shenzhen University
Shenzhen 518060, P. R. China
E-mail: huanglb@szu.edu.cn

S. Ge, F. Huang, J. He, Z. Xu, C. Pan
CAS Center for Excellence in Nanoscience
Beijing Key Laboratory of Micro-nano Energy and Sensor
Beijing Institute of Nanoenergy and Nanosystems
Chinese Academy of Sciences
Beijing 101400, P. R. China
E-mail: cfpan@binn.cas.cn

X. Han
College of Mechatronics and Control Engineering
Shenzhen University
Shenzhen 518060, P. R. China

The ORCID identification number(s) for the author(s) of this article can be found under https://doi.org/10.1002/adom.202200409.

DOI: 10.1002/adom.202200409

© 2022 Wiley-VCH GmbH

these devices are simulated successfully in a fully optical pathway. More advanced materials and innovative architectures applying in fully optical-controlled artificial synapses are imperative.

Regarding the photoresponsive materials, halide perovskites have attracted great attention because of their excellent optoelectronic properties,[14–16] and can be applied in sensor, memory, photovoltaic unit and light-emitting diode[17–20] for artificial intelligence, humanoid robotics, and flexible electronic etc.[21–33] Not only the phenomenon of negative photoresponse in halide perovskites has also been observed[34–38] but halide perovskites based synaptic devices have also been fabricated and studied.[2,39] However, most devices of those researches are based on polycrystalline perovskite film, in which the great amount of grain boundaries can cause high power consumption and gradual performances degradation ascribing to large leakage current and instability in ambient conditions, respectively. In sharp contrast to polycrystalline films, monocrystalline halide perovskites have been demonstrated with large advantages of lower trap density, higher absorption coefficients, longer carrier diffusion lengths, faster carrier mobility, and better stability, etc.[40] Therefore, monocrystalline halide perovskites affirmatively offer an ideal platform to investigate their ultimate optoelectronic properties in halide perovskite-based synaptic devices. To the best of our knowledge, only few monocrystalline halide perovskite-based synaptic devices have been reported till now.[41–43] In spite of this, the potentiation and depression of these synaptic devices are still triggered by electrical stimulation.

In addition, Zinc oxide (ZnO) as excellent electron-transport material in halide perovskite hybrid heterostructures has been demonstrated for high performance optoelectronic devices.[44–49] Importantly, ZnO possesses unique characteristics to simulate synaptic functions. Ultraviolet (UV) irradiation can induce a continuous increase of conductivity due to the desorption of chemisorbed oxygen ions on the surface of ZnO,[50] and photocurrent decays slowly after removing the UV irradiation, corresponding to the learning and forgetting processes of synapse, respectively. Therefore, perovskite-ZnO heterostructure can be a promising candidate for optoelectronic synapses.

In this work, perovskite-ZnO heterostructure with bidirectional photoresponse has been researched to realize fully optical-controlled artificial synapse. $CH_3NH_3PbBr_3$ ($MAPbBr_3$) single crystals were prepared on glass substrate by a space-limited method.[51] Then, perovskite-ZnO heterostructure was obtained by depositing a layer of ZnO. When the heterostructure was exposed to UV light and green light, the excitatory postsynaptic current (EPSC) and inhibitory postsynaptic current (IPSC) can be observed, respectively. The synaptic functions including PPF, PPD, STP-to-LTP, STD-to-LTD, and learning-experience behavior were mimicked successfully. Besides, potentiation and depression were triggered consecutively, demonstrating the reliability and repeatability of the fully optical-controlled synapse. Logic functions such as "OR," "AND," "NOR," and "NAND," have also been realized by the optoelectronic synapse. These results underscore the potential of such perovskite-ZnO heterostructure for application in fully optical-controlled neuromorphic systems.

2. Results and Discussion

To realize the single crystal perovskite-ZnO heterostructure, we first investigate the preparation of single crystal perovskites, as shown in **Figure 1**. The space-limited solvent evaporation crystallization method for the fabrication of $MAPbBr_3$ single crystals is depicted in Figure 1a. The precursor solution is added into the gap of hydrophobic and hydrophilic glasses via capillarity effect and then heated at 80 °C until the formation of millimeter-scale single crystals.[51] The optical photograph and scanning electron microscopy (SEM) image in Figure 1b presents a smooth surface of $MAPbBr_3$ single crystal without grain boundaries. More optical photographs of different samples are provided in Figure S1, Supporting Information. Energy-dispersive X-ray spectroscopy (EDS) mapping images in Figure 1b confirm the uniform Pb and Br elements distribution. Atomic force microscope (AFM) image in Figure 1c further identifies the flat surface of $MAPbBr_3$ single crystal with a root mean square roughness of ≈0.99 nm. XRD pattern with strong (h00) peaks proves the cubic lattice structure (inset in Figure 1d) and high crystal quality of $MAPbBr_3$ single crystal in Figure 1d. The thicknesses of most single crystals are ≈5.0 μm (Figure 1e) in the reference of the statistical results in Figure S2, Supporting Information. The ultraviolet-visible (UV–vis) absorption spectrum of $MAPbBr_3$ single crystal in Figure 1f (black curve) shows an obvious band edge cutoff at around 550 nm, suggesting few in-gap defect states.[52] Meanwhile, the optical band gaps of 2.25 eV are calculated in the upper inset of Figure 1f. As shown in Figure 1f (orange curve) and lower inset, a narrow photoluminescence (PL) peak near the absorption band edge and a typical fluorescence image of single crystal can be observed, respectively, attributing to the intrinsic PL of $MAPbBr_3$ crystal lattice. PL decay curve of $MAPbBr_3$ single crystal excited by a 375 nm laser in Figure 1g exhibits the carrier recombination behaviors, which possesses two components of fast (1.27 ns) and slow (9.24 ns) dynamics by a biexponential function fitting, regarded as the carrier lifetimes of surface and bulk recombination, respectively.[43]

After the preparation of $MAPbBr_3$ single crystal, ZnO film was deposited on the surface of single crystal to form perovskite-ZnO heterostructure. The thickness of ZnO film is ≈30 nm as displayed in the cross-sectional SEM image of the perovskite-ZnO heterostructure (Figure S3, Supporting Information). The characteristic peak at 34.4° shown in XRD spectrum of ZnO (Figure S4a, Supporting Information) is indexed to the (002) crystal planes of wurtzite phase,[50] which cannot be observed in XRD pattern of perovskite-ZnO heterostructure in Figure S4b, Supporting Information. This can be attributed two reasons, one is the (h00) peaks of $MAPbBr_3$ single crystal are too strong and the other one is the relatively thin thickness of ZnO film (≈30 nm) with the weak XRD peak. To characterize the optical properties of perovskite-ZnO heterostructure, the absorption spectra were recorded in Figure S5a, Supporting Information, demonstrating the typical UV absorption of ZnO at wavelength shorter than 380 nm, while it also shows the absorption edge of $MAPbBr_3$ single crystal in the absorption spectrum of perovskite-ZnO heterostructure. Furthermore, by fitting PL decay curve in Figure S5b, Supporting Information, perovskite-ZnO heterostructure presents faster decay and shorter lifetime than that of $MAPbBr_3$ single crystal, which may be attributed to the exciton separation between $MAPbBr_3$ and ZnO interface.[9]

© 2022 Wiley-VCH GmbH

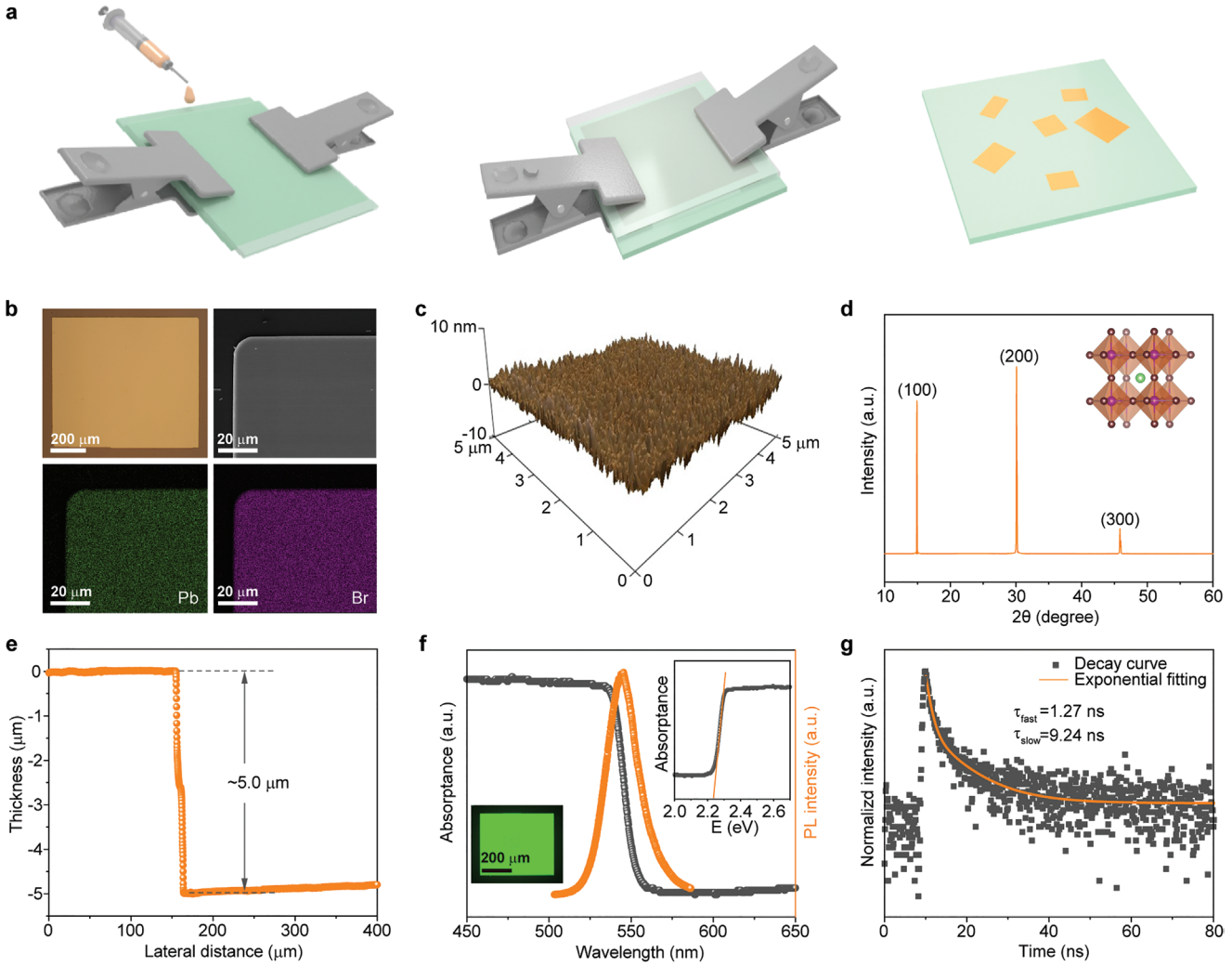

Figure 1. a) Schematic diagram of $MAPbBr_3$ single crystal growth. b) Optical photograph, SEM, and EDS mapping images of Pb and Br elements distribution. c) 3D AFM image of the $MAPbBr_3$ single crystal. d) XRD pattern of the $MAPbBr_3$ single crystal. Inset is the corresponding crystal structure. e) The thickness of the $MAPbBr_3$ single crystal. f) Optical absorption and PL spectrum of the $MAPbBr_3$ single crystal. Insets are the fluorescence image and spectrum of absorbance versus photon energy. g) PL decay profile of $MAPbBr_3$ single crystal excited by a 375 nm laser.

Figure 2a schematically shows a synaptic device based on the perovskite-ZnO heterostructure. Based on the remarkable UV photoresponse of ZnO, the basic synaptic behaviors of perovskite-ZnO heterostructure are studied, while the photoresponsive current is regarded as the EPSC and the current change is represented with ΔEPSC. Herein, the common 365 nm UV light source was applied to perform the measurement. Figure S6a, Supporting Information depicts current versus voltage (*I*–*V*) curves of perovskite-ZnO heterostructure at different UV light intensities, proving the intensity dependence of photocurrent. Moreover, a typical current evolution process in Figure 2b exhibits a continuous increase of EPSC with prolonged UV light irradiation for 100 s. This can be mainly ascribed to the persistent increase of photogenerated electrons under UV light irradiation because the photogenerated holes discharge the chemisorbed oxygen ions on the surface of ZnO, remaining photogenerated electrons.[53] It is proposed that desorption of oxygen ions dominates the conductance of perovskite-ZnO heterostructure under UV light irradiation and the role of photogenerated carriers from $MAPbBr_3$ is weak. The changes of EPSC are also recorded with different light intensities and illuminating time in Figure S6b, Supporting Information, revealing that the higher the UV light intensities or the longer the illuminating time are, the larger the EPSC increases. After the removal of UV light, the EPSC gradually decays and this also can be observed in current evolution processes at different light intensities and their corresponding decay curves (Figure S6c,d, Supporting Information). The decay curves can be fitted well with the double-exponential function:

$$I = I_1 \exp\left(-\frac{t}{\tau_1}\right) + I_2 \exp\left(-\frac{t}{\tau_2}\right) \quad (1)$$

where the characteristic relaxation time of τ_1 and τ_2 are related to the rapid band-to-band recombination and slow defect

© 2022 Wiley-VCH GmbH

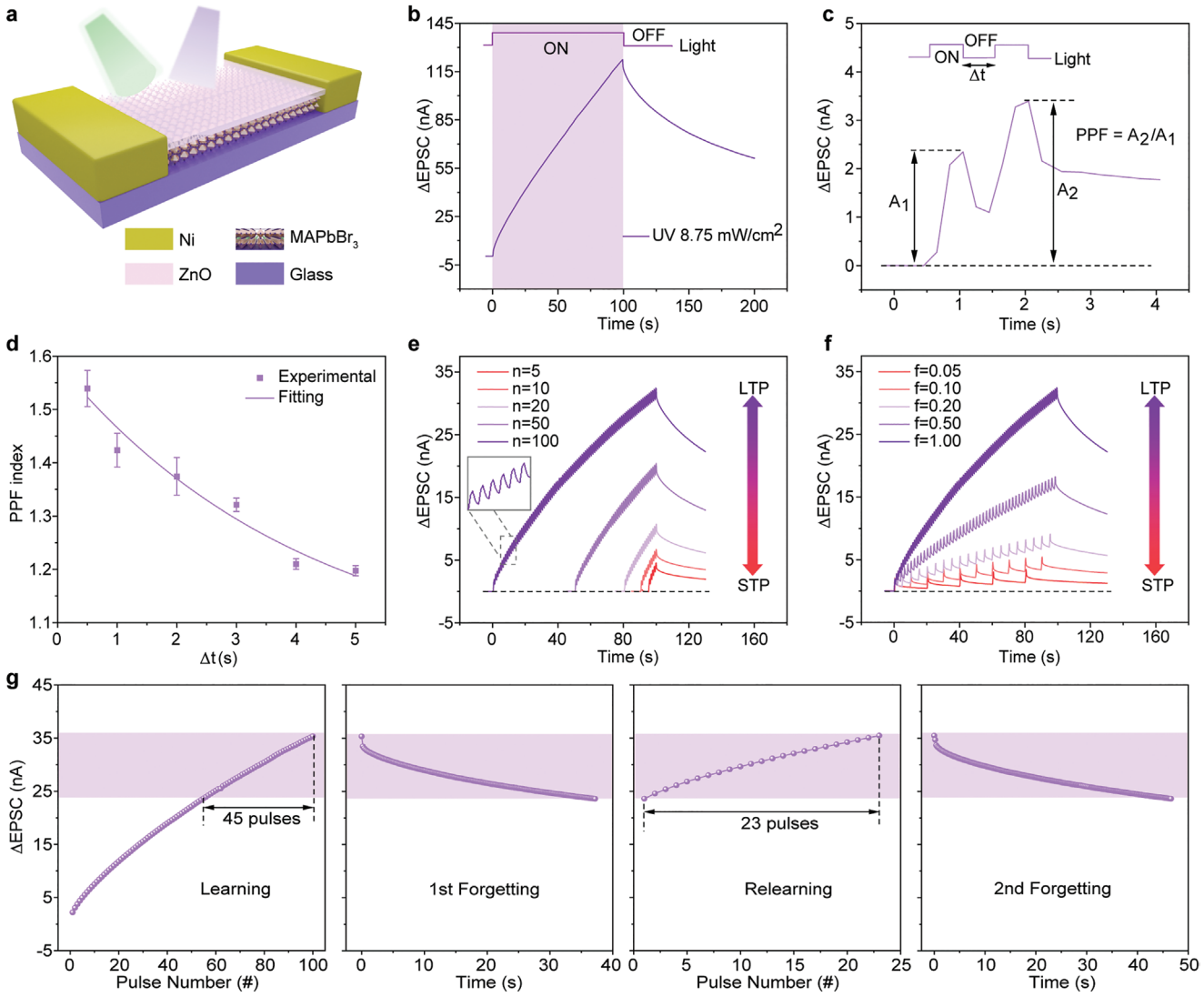

Figure 2. a) The schematic of the synaptic device. b) Current evolution process of 365 nm UV light stimuli with an intensity of 8.75 mW cm^{-2} for 100 s. c) EPSC of the synaptic device triggered by a pair of UV light pulses with 0.5 s pulse duration and 0.5 s pulse interval. d) Variation of PPF index with different interval times (Δt) of two pulses fitted by an exponential function. The fixed duration time of pulses is 0.5 s. e) STP-to-LTP transition by increasing the UV light pulse number with 0.5 s pulse duration and 0.5 s pulse interval. The inset is zoom-in curve. f) STP-to-LTP transition by increasing the UV light pulse frequency with 0.5 s pulse duration. g) Learning-experience behavior including learning, forgetting, and relearning processes with 0.5 s pulse duration and 0.5 s pulse interval. Light intensity in (c–g): 3.45 mW cm^{-2}.

states recombination of photogenerated electron-hole pairs, respectively.[50]

Continuous increase of conductivity under UV exposure and slow decay of photocurrent by removing the UV light are essential for the realization of optical-controlled learning and forgetting processes of synaptic devices. Furthermore, pulsed UV light stimuli as presynaptic spike have also been employed to investigate excitatory behaviors of synapse. As seen in Figure 2c,a pair of light pulses with the pulse duration of 0.5 s and interval of 0.5 s was applied, in which the EPSC evoked by the second light pulse (A_2) is larger than the EPSC triggered by the first light pulse (A_1), known as the synaptic plasticity called PPF. PPF index that can be described by the ratio of A_2 to A_1, denotes the enhancement extent of EPSC and is critically related to the interval time. Figure 2d presents the variation of PPF index with different interval times between two light pulses. As the increase of pulse interval time, the PPF index exponentially decays, which is consistent with the learning rules of biological synapse.[39]

By modulating the device conductivity, that is, synaptic weight, the synaptic plasticity of STP and LTP can be mimicked. STP accords with the weak and temporal potentiation of synaptic weight and can be transformed to strong and permanent potentiation named LTP after repetitive training. Herein, the STP-to-LTP transition has also been demonstrated by increasing the number or frequency of UV light pulse as presented in Figure 2e,f, respectively. Obviously, the pulse stimulation with the more pulse number (n) or the higher pulse frequency (f) can trigger stronger potentiation of synaptic weight, also result a longer decay time of EPSC shown in Figure S7, Supporting

© 2022 Wiley-VCH GmbH

Information representing the more permanent potentiation. As known in human brains, relearning the forgotten information always needs less time or training than the case of the first learning, namely learning-experience behavior. Therefore, this learning phenomenon was also proved as displayed in Figure 2g. The first learning process was stimulated by 100 consecutive light pulses. After the removal of light stimulation, the EPSC decayed spontaneously corresponding to the first forgetting process. When the EPSC decayed to an intermediate level, light pulses were reapplied to recover the potentiation. Interestingly, compared to the 45 pulses needed in the first learning process, only 23 pulses were enough for relearning to identical potentiation. In contrast, the second forgetting process needed a longer time than that of the first forgetting process, indicating the enhancement of the potentiation in relearning process. As a result, the learning-experience behavior of human brains was well mimicked by the heterostructure-based synaptic device. In addition, the learning and forgetting processes are corelated with the response time of photocurrent under illumination and recovery time of photocurrent in dark, respectively. The response time was introduced as the interval time from 10% to 90% of max ΔEPSC,[54] as well as the recovery time. After the stimulus of UV light pulse with duration time of 1.0 s, the average response time (≈0.70 s) and recovery time (≈11.51 s) of five devices were evaluated as shown in Figure S8, Supporting Information, respectively.

Figure 3a is the schematic illustration of biological neuron and synapse. Their activities are performed by releasing excitatory or inhibitory neurotransmitters on the presynaptic neuron under stimulation and binding the receptors on the postsynaptic neuron to induce EPSC or IPSC, respectively. As discussed above, the excitatory behaviors of synapse have been simulated successfully by UV light stimuli due to the positive photoresponse of perovskite-ZnO heterostructure. In order to the realization of fully optical controlled artificial synapses, based on negative photoresponse to mimic the inhibitory behavior is imperative. Excitedly, negative photoresponse can be observed while this synaptic device is illuminated with green light, and with prolonged exposure of green light for 100 s, the IPSC is continuously decreasing, as seen in Figure 3b. A larger light intensity is applied for an obvious phenomenon of negative photoresponse. Similarly, the change of inhibitory current is represented with ΔIPSC. Noteworthily, the measurements of negative photoresponse, that is, the inhibitory behaviors were based on a prior UV light stimulus for a high device conductivity (μA level). A high device conductivity can present a widely adjustable range for the negative photoresponse. The phenomenon of negative photoresponse can be suggested with the decrease of effective transport carriers that is caused by the formation of a deeper depletion layer between perovskite and ZnO interface due to the diffusion of photogenerated carriers. The diffused dynamics of negative photoresponse has been reported in $CH_3NH_3PbBr_3$-ZnO microbelt.[36] It should be noted that the photogenerated carriers are mainly derived from perovskite instead of ZnO under green light illumination because of the weak visible light absorption and photoresponse of ZnO. Prolonged the green light exposure induces a deeper and deeper depletion layer resulting in a smaller and smaller current. After the removal of green light illumination, the IPSC gradually recovers attributed to the recombination of photogenerated electron-hole pairs in perovskite. IPSC depends on the green light intensities and illuminating time. The higher light intensity or longer illuminating time causes a smaller IPSC, as illustrated in Figure 3c. This contrasts to the larger EPSC triggered by the higher UV light intensity or longer illuminating time. Furthermore, benefiting from the broad absorption of perovskite in visible light region, blue (460 nm) or violet (420 nm) light also can induce the decrease of IPSC with the longer illuminating time, as seen in Figure 3d.

Similarly, pulsed green light stimuli have also been employed to investigate the inhibitory behaviors of synapse. Compared with the PPF trigged by the UV light pulses which is referred to as the potentiation of synaptic weight, the PPD trigged by the green light pulses shows the depression of synaptic weight. As shown in Figure 3e, the IPSC evoked by the second light pulse (A_2) is smaller than the IPSC triggered by the first light pulse (A_1) when a pair of green light pulses with the pulse duration of 0.5 s and time interval of 0.5 s was applied. PPD index as reduction extent of IPSC also exhibits tendency of exponential decay with the increase of interval time between two light pulses in Figure 3f. Afterward, the STD-to-LTD transition has been proved by increasing the number (n) or frequency (f) of green light pulse in Figure 3g,h, respectively. Apparently, the pulse stimulation with the more pulse number or the higher pulse frequency can trigger the stronger depression of synaptic weight and their corresponding recovery curves are shown in Figure S9, Supporting Information. The different degrees of PPF and PPD decay characteristics, as well as the decay curves and recovery curves in Figures S7 and S9, Supporting Information, can be related with the different photoresponsive mechanisms and light intensity under UV and green light irradiation, respectively.

Therefore, based on the bidirectional photoresponse in perovskite-ZnO heterostructure, both the excitatory and inhibitory behaviors are emulated successfully. The mechanism of bidirectional photoresponse is proposed with the increase of photogenerated electrons ascribing to the desorption of oxygen ions on the ZnO surface and the decrease of transport carriers owing to the formation of the deeper depletion layer. Generally, $MAPbBr_3$ as p-type conductivity can be assembled in a typical p-n heterojunction with the n-type ZnO.[36] Meanwhile, a built-in electric field was formed at the depletion layer. While the UV light was applied to the heterojunction, the photogenerated holes of ZnO can discharge the chemisorbed oxygen ions, remaining photogenerated electrons and causing positive photoresponse. The photogenerated electrons dominate the conductance of perovskite-ZnO heterostructure. With the exposure of green light, photogenerated holes in perovskite and electrons in ZnO will further diffuse to form a deeper depletion layer (Figure S10, Supporting Information) resulting in the reduction of effective transport carriers and the phenomenon of negative photoresponse. Although the perovskite can also respond the UV light as seen in Figure S11a, Supporting Information and the diffusion of photogenerated holes may lead to a deeper depletion layer and reduction of effective transport carriers in the same way. It should be noted that the effect of reduction of effective carriers inducing by UV photoresponse of perovskite is weak. This may be related to the more UV

© 2022 Wiley-VCH GmbH

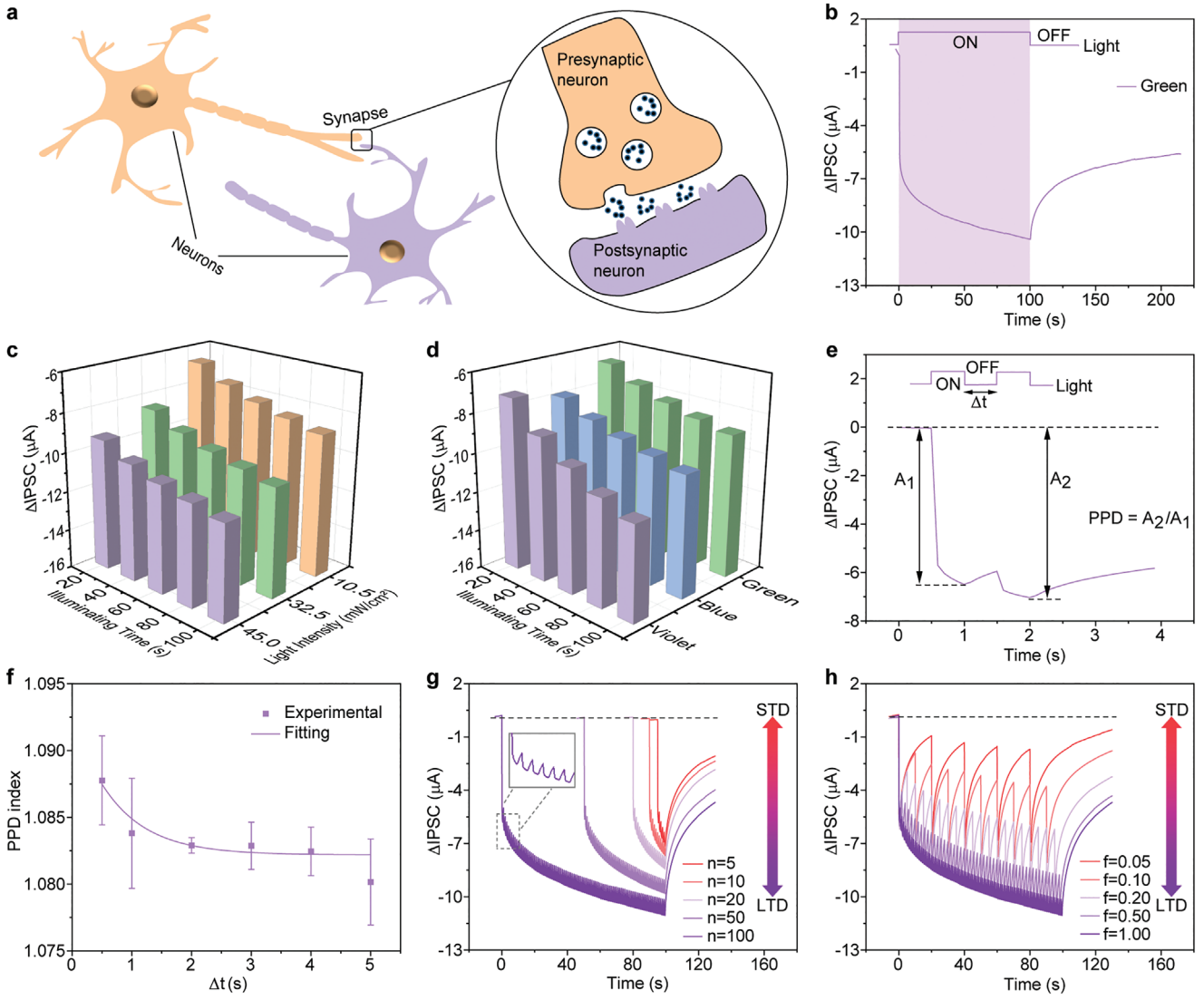

Figure 3. a) Schematic illustration of neuron and synapse. b) Current evolution process of 520 nm green light stimuli with an intensity of 32.5 mW cm^{-2} for 100 s. c) The changes of IPSC relying on illuminating time at different intensities of green light. d) The changes of IPSC relying on illuminating time under green, blue and violet light, respectively. e) IPSC of the synaptic device triggered by a pair of green light pulses with 0.5 s pulse duration and 0.5 s pulse interval. f) Variation of PPD index with different interval time (Δt) of two pulses fitted by an exponential function. The fixed duration time of pulse is 0.5 s. g) STD-to-LTD transition by increasing the green light pulse number with 0.5 s pulse duration and 0.5 s pulse interval. The inset is zoom-in curve. h) STD-to-LTD transition by increasing the green light pulse frequency with 0.5 s pulse duration. Light intensity in (e–h): 32.5 mW cm^{-2}.

light was absorbed by ZnO than the absorption by the covered perovskite as illustrated in transmittance spectrum of ZnO (Figure S12, Supporting Information), numerous remaining photogenerated electrons were generated than the number of diffused electrons. Meanwhile, the better transmittance can be observed in the longer wavelength, indicating that the green light may be more suitable than the blue and violet light for the characterization of the perovskite-ZnO heterostructure. More green light can be absorbed by the perovskite resulting in the change of depletion layer in perovskite-ZnO heterostructure for an obvious negative photoresponse. Herein, the ZnO film was prepared for a same thickness, because the thickness of ZnO can affect the transmittance of both UV and green light, as well as the synaptic behavior. The UV photoresponse and synaptic behaviors of individual ZnO have also been verified in Figure S11b–d, Supporting Information, and the ZnO is basically unresponsive to the green light illumination (inset in Figure S11b, Supporting Information). Certainly, with prolonged light illumination time, the negative and positive photocurrent can continuously decrease or increase, corresponding to the deeper and deeper depletion layer and more and more oxygen ions desorption, respectively.

Subsequently, to further investigate the fully optical-controlled artificial synapse, consecutive potentiation, and depression behaviors by stimulating with different light pulses are demonstrated in **Figure 4**a,b. After ×50 UV light pulses were applied onto the heterostructure to trigger the EPSC, ×25 green light pulses were followed to induce the IPSC. The change from

© 2022 Wiley-VCH GmbH

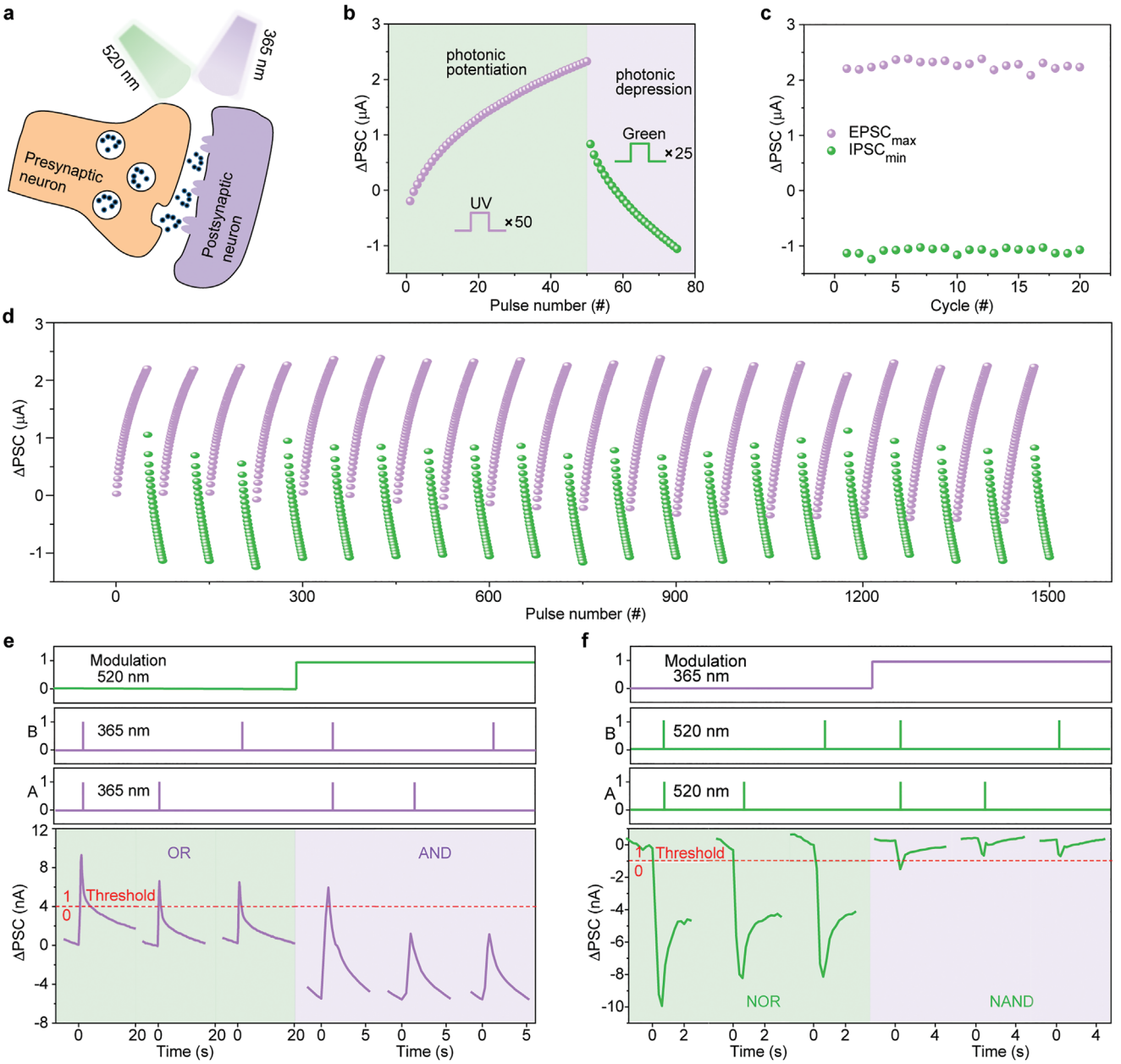

Figure 4. a) Schematic illustration of the fully optical-controlled synapse. b) Potentiation and depression by stimulating with ×50 UV light pulses and ×25 green light pulses, respectively. Both the pulse duration and pulse interval are 0.5 s. c) Variation of the $EPSC_{max}$ and $IPSC_{min}$ from initial to 20 cycles. d) Cyclic potentiation and depression for 20 cycles. e) Simulation of "OR" and "AND" logic functions by using UV light as inputs A and B, green light as modulatory input. f) Simulation of "NOR" and "NAND" logic functions by using green light as inputs A and B, UV light as modulatory input. UV light intensity: 3.45 mW cm^{-2} and green light intensity: 32.5 mW cm^{-2}.

potentiation to depression reveals the fully optical-controlled characteristics. Furthermore, the small variation of the $EPSC_{max}$ and $IPSC_{min}$ and the cyclic potentiation and depression for 20 cycles prove the reliable and repeatable performance without noticeable degradation as displayed in Figure 4c,d, respectively, which is comparable and even prominent than other fully optical-controlled devices in **Table 1**. Notably, the EPSC shows a greater enhancement under the stimulation of UV light pulses than that in the pristine device as seen in Figure 2. The prior UV light stimulus for excitatory behavior with high device conductivity (μA level) induced a shallower depletion layer that may be responsible.

Finally, by a prior UV light stimulus for a sub-microamp level conductivity, the logic functions of "OR," "AND," "NOR," and "NAND" were achieved based on the fully optical-controlled heterostructure. Figure S13, Supporting Information presents the truth tables of the logic functions, including two inputs A and B, a modulatory input and an output. Input A, B and modulation correspond to different light sources and the light on and off represent the input signals "1" and "0,"

© 2022 Wiley-VCH GmbH

Table 1. Comparison of fully optical-controlled artificial synapse.

Device Structure[a)]	Light source [nm]		PPF/PPD	STP-LTP STD-LTD	Rep.	Ref.
	EPSC	IPSC				
Pyr-GDY/Gr/PbS	980	450	√	√	10	[5]
O_D-IGZO/O_R-IGZO	420	800	–	–	10	[10]
Bi_2O_2Se/Graphene	635	365	√	√	3	[6]
ZnO/PbS/ZnO	365	980	√	√	–	[9]
Black Phosphorus	280	365	–	√	1	[11]
Black Phosphorus	280	365	√	√	–	[12]
Black Phosphorus	280	365	√	√	–	[13]
Perovskite/ZnO	365	520	√	√	20	This work

[a)]Symbols "√" and "–" denote given and not given, respectively. Rep.: Repeatability. Ref.: Reference. Pyr-GDY: pyrenyl graphdiyne. Gr: graphene. O_D-IGZO: oxygen-deficient InGaZnO. O_R-IGZO: oxygen-rich InGaZnO.

respectively. The modulatory input plays an important role in modulating the output current level for the achievement of different logic functions. The output signal "1" and "0" indicate whether the output current exceeds the threshold. In Figure 4e,a green light source as modulatory input and two UV light sources as inputs A and B, were used to realize "OR" and "AND" functions. While the input signal of modulation is "0," that is, the green light source is switched off, all of the three conditions, input A "1" and input B "1," input A "1" and input B "0," input A "0" and input B "1," can trigger the output signal of "1," demonstrating "OR" logic function. While the input signal of modulation is "1," that is, the green light source is switched on to induce a negative photoresponse behavior for a lower current level, only the condition of input A "1" and input B "1" can trigger the output signal of "1," demonstrating "AND" logic function. Similarly, by using a UV light source as modulatory input and two green light sources as inputs A and B in Figure 4f, "NOR" and "NAND" logic functions have also been proved. Based on the unrecovered current level in the simulation of "NOR" function by the green light illumination, the UV light source is switched on for a positive photoresponse behavior to recover the current level for the simulation of "NAND" function. The generated energy consumption of each light stimulus is less than 0.5 nJ spike^{-1} under the 0.1 V, 0.5 s pulse, and the UV and green light power consumption is ≈1.8 and ≈17.1 μJ on effective device area (≈700 × 150 μm^2), respectively. The logic functions are realized by fully optical stimuli instead of electrical stimuli or coupled electrical and optical stimuli, indicating the application possibility of the optoelectronic devices. Furthermore, a preliminary simulation of pattern recognition and a representative imaging array was performed to demonstrate the more possibility of the perovskite-ZnO heterostructure for neuromorphic computation. The method of hardware-based backpropagation (BP) algorithm was employed to calculate and update the synaptic weight.[55] After a training process, the outline of figure can be observed indistinctly in the mapping image, and the recognition rate is ≈80% as seen in Figure S14, Supporting Information. By 10 s UV light stimulus on a representative imaging array in Figure S15, Supporting Information, the currents were measured after removing the light illumination for 15, 30, and 60 s. The image still can be distinguished at the decay time of 30 s, indicating the proof-of-concept image recognition and storage.

3. Conclusion

In summary, $MAPbBr_3$ single crystals with high crystal quality were prepared by a space-limited solvent evaporation method, and further assembled with ZnO in perovskite-ZnO heterostructure. The heterostructure exhibited positive and negative photoresponse while exposed to UV and green light illumination, respectively. Based on this heterostructure, various functions of synapse were simulated successfully, such as PPF, PPD, STP-to-LTP, STD-to-LTD. Fully optical-controlled features were demonstrated by consecutive UV light and green light stimuli, revealing reliable and repeatable performance. Meanwhile, the logic functions including "OR," "AND," "NOR," and "NAND" were achieved by modulating UV and green light illumination. To the best of our knowledge, this perovskite-ZnO heterostructure is the first example of halide perovskite based fully optical-controlled artificial synapse, and the study paves the way toward fully optical-controlled devices. A high-density device array with stable and lead-free perovskite structure may make it possible for the future application of neuromorphic systems.

4. Experimental Section

Preparation of $MAPbBr_3$ Single Crystals: The precursor solution of $MAPbBr_3$ was prepared by stirring MABr and $PbBr_2$ (1.1 M) in N, N-dimethylformamide (DMF) solvent for 1 h at room temperature. Then, one glass substrate was treated by oxygen plasma cleaner for 300 s at 100 W to form a hydrophilic surface. Another glass substrate was treated by a mixed solution of hexane and (octadecyl)trichlorosilane (OTS) with the ratio of 200:1 for 20 min, followed by acetone and deionized water rinsing to form a hydrophobic surface. Finally, the hydrophobic and hydrophilic glasses were clipped together and the precursor solution was added into the gap of two glasses via capillarity effect, heated at 80 °C for the formation of $MAPbBr_3$ single crystals.

Characterization: The optical photograph, SEM, and EDS images were obtained by using the optical microscope (Zeiss Observer Z1) and SEM (FEI Nova NanoSEM 450), respectively. AFM (Asylum Research

© 2022 Wiley-VCH GmbH

MFP-3D-SA), XRD (PANalytical X'Pert3), and Step Profiler (KLA-Tencor P7) were used to measure the surface roughness, lattice structure, and thickness, respectively. The absorption spectra were detected by Shimadzu UV 3600. The PL spectrum and PL decay curve were recorded by steady-state/transient fluorescence spectrometer (FLS980).

Device Fabrication and Measurements: After the preparation of $MAPbBr_3$ single crystals, ZnO film was deposited on the surface of perovskite to form the perovskite-ZnO heterostructure by RF magnetron sputtering (PVD75 Kurt J. Lesker) under the conditions of 25 sccm Ar, 60 W power, and 30 min time. Low-cost non-precious Ni electrode with high adhesion was also deposited by the magnetron sputtering successively through a shadow mask with a channel width of 150 µm. The electrical and optoelectronic properties were measured with Keysight Technologies B1500A Semiconductor Device Analyzer. Both the continuous light illumination and pulsed light stimuli were introduced by an arbitrary/function generator (Tektronix AFG3011C) to drive corresponding light-emitting diodes.

Supporting Information

Supporting Information is available from the Wiley Online Library or from the author.

Acknowledgements

The authors thank the support of National Natural Science Foundation of China (No. 52125205, U20A20166, 51973119, 61805015, and 61804011), Natural Science Foundation of Beijing Municipality (Z180011), The Natural Science Foundation of GuangDong Province (2019A1515011566 and 2018A0303130060), GuangDong Natural Science Foundation under Grant (2019B1515120042), Shenzhen Science and Technology Program (Grant No. KQTD20170810105439418), and the Fundamental Research Funds for the Central Universities.

Conflict of Interest

The authors declare no conflict of interest.

Data Availability Statement

Research data are not shared.

Keywords

artificial synapses, bidirectional photoresponse, fully optical-controlled synapses, halide perovskites, ZnO

Received: February 20, 2022
Published online:

[1] Q.-B. Zhu, B. Li, D.-D. Yang, C. Liu, S. Feng, M.-L. Chen, Y. Sun, Y.-N. Tian, X. Su, X.-M. Wang, S. Qiu, Q.-W. Li, X.-M. Li, H.-B. Zeng, H.-M. Cheng, D.-M. Sun, *Nat. Commun.* **2021**, *12*, 1798.
[2] R. A. John, N. Yantara, S. E. Ng, M. I. B. Patdillah, M. R. Kulkarni, N. F. Jamaludin, J. Basu, Ankit, S. G. M. , A. Basu, N. Mathews, *Adv. Mater.* **2021**, *33*, 2007851.
[3] H. Liu, Q. Hua, R. Yu, Y. Yang, T. Zhang, Y. Zhang, C. Pan, *Adv. Funct. Mater.* **2016**, *26*, 5307.
[4] J. Zhang, S. Dai, Y. Zhao, J. Zhang, J. Huang, *Adv. Intell. Syst.* **2020**, *2*, 1900136.
[5] Y.-X. Hou, Y. Li, Z.-C. Zhang, J.-Q. Li, D.-H. Qi, X.-D. Chen, J.-J. Wang, B.-W. Yao, M.-X. Yu, T.-B. Lu, J. Zhang, *ACS Nano* **2021**, *15*, 1497.
[6] C.-M. Yang, T.-C. Chen, D. Verma, L.-J. Li, B. Liu, W.-H. Chang, C.-S. Lai, *Adv. Funct. Mater.* **2020**, *30*, 2001598.
[7] Y. Shen, N. C. Harris, S. Skirlo, M. Prabhu, T. Baehr-Jones, M. Hochberg, X. Sun, S. Zhao, H. Larochelle, D. Englund, M. Soljačić, *Nat. Photonics* **2017**, *11*, 441.
[8] Z. Cheng, C. Ríos, W. H. P. Pernice, C. D. Wright, H. Bhaskaran, *Sci. Adv.* **2017**, *3*, e1700160.
[9] H. Li, X. Jiang, W. Ye, H. Zhang, L. Zhou, F. Zhang, D. She, Y. Zhou, S.-T. Han, *Nano Energy* **2019**, *65*, 104000.
[10] L. Hu, J. Yang, J. Wang, P. Cheng, L. O. Chua, F. Zhuge, *Adv. Funct. Mater.* **2021**, *31*, 2005582.
[11] T. Ahmed, M. Tahir, M. X. Low, Y. Ren, S. A. Tawfik, E. L. H. Mayes, S. Kuriakose, S. Nawaz, M. J. S. Spencer, H. Chen, M. Bhaskaran, S. Sriram, S. Walia, *Adv. Mater.* **2021**, *33*, 2004207.
[12] T. Ahmed, S. Kuriakose, S. Abbas, M. J. S. Spencer, M. A. Rahman, M. Tahir, Y. Lu, P. Sonar, V. Bansal, M. Bhaskaran, S. Sriram, S. Walia, *Adv. Funct. Mater.* **2019**, *29*, 1901991.
[13] T. Ahmed, S. Kuriakose, E. L. H. Mayes, R. Ramanathan, V. Bansal, M. Bhaskaran, S. Sriram, S. Walia, *Small* **2019**, *15*, 1900966.
[14] J. Sun, N. Li, L. Dong, X. Niu, M. Zhao, Z. Xu, H. Zhou, C. Shan, C. Pan, *Nanotechnology* **2021**, *32*, 475204.
[15] J. Sun, Q. Hua, M. Zhao, L. Dong, Y. Chang, W. Wu, J. Li, Q. Chen, J. Xi, W. Hu, C. Pan, C. Shan, *Adv. Mater. Technol.* **2021**, *6*, 2100229.
[16] J. Sun, Q. Hua, R. Zhou, D. Li, W. Guo, X. Li, G. Hu, C. Shan, Q. Meng, L. Dong, C. Pan, Z. L. Wang, *ACS Nano* **2019**, *13*, 4507.
[17] R. Bao, C. Wang, L. Dong, C. Shen, K. Zhao, C. Pan, *Nanoscale* **2016**, *8*, 8078.
[18] H. Liu, X. Chen, Y. Zheng, D. Zhang, Y. Zhao, C. Wang, C. Pan, C. Liu, C. Shen, *Adv. Funct. Mater.* **2021**, *31*, 2008006.
[19] M. Que, W. Guo, X. Zhang, X. Li, Q. Hua, L. Dong, C. Pan, *J. Mater. Chem. A* **2014**, *2*, 13661.
[20] Y. Peng, J. Lu, D. Peng, W. Ma, F. Li, Q. Chen, X. Wang, J. Sun, H. Liu, C. Pan, *Adv. Funct. Mater.* **2019**, *29*, 1905051.
[21] K. Zhou, Y. Zhao, X. Sun, Z. Yuan, G. Zheng, K. Dai, L. Mi, C. Pan, C. Liu, C. Shen, *Nano Energy* **2020**, *70*, 104546.
[22] H. Liu, Q. Li, Y. Bu, N. Zhang, C. Wang, C. Pan, L. Mi, Z. Guo, C. Liu, C. Shen, *Nano Energy* **2019**, *66*, 104143.
[23] C. Wang, C. Pan, Z. Wang, *ACS Nano* **2019**, *13*, 12287.
[24] H. Zhang, D. Peng, W. Wang, L. Dong, C. Pan, *J. Phys. Chem. C* **2015**, *119*, 28136.
[25] K. Zhou, W. Xu, Y. Yu, W. Zhai, Z. Yuan, K. Dai, G. Zheng, L. Mi, C. Pan, C. Liu, C. Shen, *Small* **2021**, *17*, 2100542.
[26] J. Sun, Y. Chang, L. Dong, K. Zhang, Q. Hua, J. Zang, Q. Chen, Y. Shang, C. Pan, C. Shan, *Nano Energy* **2021**, *86*, 106077.
[27] E. Li, Y. Pan, C. Wang, C. Liu, C. Shen, C. Pan, X. Liu, *ACS Appl. Mater. Interfaces* **2021**, *13*, 28996.
[28] E. Li, Y. Pan, C. Wang, C. Liu, C. Shen, C. Pan, X. Liu, *Chem. Eng. J.* **2021**, *420*, 129864.
[29] C. Wang, J. Zhao, C. Ma, J. Sun, L. Tian, X. Li, F. Li, X. Han, C. Liu, C. Shen, L. Dong, J. Yang, C. Pan, *Nano Energy* **2017**, *34*, 578.
[30] R. Yu, C. Pan, O. J. Guy, L. Dong, M. Tonezzer, *J. Nanomater.* **2016**, *2016*, 9162634.
[31] C. Wang, D. Peng, J. Zhao, R. Bao, T. Li, L. Tian, L. Dong, C. Shen, C. Pan, *Small* **2016**, *12*, 5734.
[32] X. Wang, H. Zhang, R. Yu, L. Dong, D. Peng, A. Zhang, Y. Zhang, H. Liu, C. Pan, Z. L. Wang, *Adv. Mater.* **2015**, *27*, 2324.
[33] R. Yu, L. Dong, C. Pan, S. Niu, H. Liu, W. Liu, S. Chua, D. Chi, Z. L. Wang, *Adv. Mater.* **2012**, *24*, 3532.

© 2022 Wiley-VCH GmbH

[34] M. A. Haque, J.-L. Li, A. L. Abdelhady, M. I. Saidaminov, D. Baran, O. M. Bakr, S.-H. Wei, T. Wu, *Adv. Opt. Mater.* **2019**, *7*, 1900865.
[35] Y. Kim, B. Park, *Nanoscale* **2018**, *10*, 20377.
[36] F. Chen, Z. Shi, J. Chen, Q. Cui, A. Jian, Y. Zhu, Q. Xu, Z. Lou, C. Xu, *Appl. Phys. Lett.* **2021**, *118*, 171901.
[37] N. K. Tailor, P. Maity, M. I. Saidaminov, N. Pradhan, S. Satapathi, *J. Phys. Chem. Lett.* **2021**, *12*, 2286.
[38] N. K. Tailor, P. Maity, S. Satapathi, *ACS Photonics* **2021**, *8*, 2473.
[39] L. Yin, W. Huang, R. Xiao, W. Peng, Y. Zhu, Y. Zhang, X. Pi, D. Yang, *Nano Lett.* **2020**, *20*, 3378.
[40] D. Peng, X. Liu, C. Pan, *Sci. Bull.* **2021**, *66*, 6.
[41] H. Tian, L. Zhao, X. Wang, Y.-W. Yeh, N. Yao, B. P. Rand, T.-L. Ren, *ACS Nano* **2017**, *11*, 12247.
[42] J.-Y. Mao, Z. Zheng, Z.-Y. Xiong, P. Huang, G.-L. Ding, R. Wang, Z.-P. Wang, J.-Q. Yang, Y. Zhou, T. Zhai, S.-T. Han, *Nano Energy* **2020**, *71*, 104616.
[43] J. Gong, H. Yu, X. Zhou, H. Wei, M. Ma, H. Han, S. Zhang, Y. Ni, Y. Li, W. Xu, *Adv. Funct. Mater.* **2020**, *30*, 2005413.
[44] P. Zhang, J. Wu, T. Zhang, Y. Wang, D. Liu, H. Chen, L. Ji, C. Liu, W. Ahmad, Z. D. Chen, S. Li, *Adv. Mater.* **2018**, *30*, 1703737.
[45] R. Bao, C. Wang, Z. Peng, C. Ma, L. Dong, C. Pan, *ACS Photonics* **2017**, *4*, 1344.
[46] X. Zhao, R. Zhou, Q. Hua, L. Dong, R. Yu, C. Pan, *J. Nanomater.* **2015**, *2015*, 7.
[47] C. Wang, R. Bao, K. Zhao, T. Zhang, L. Dong, C. Pan, *Nano Energy* **2015**, *14*, 364.
[48] R. Bao, C. Wang, L. Dong, R. Yu, K. Zhao, Z. L. Wang, C. Pan, *Adv. Funct. Mater.* **2015**, *25*, 2884.
[49] C. Pan, W. Guo, L. Dong, G. Zhu, Z. L. Wang, *Adv. Mater.* **2012**, *24*, 3356.
[50] W. Xiao, L. Shan, H. Zhang, Y. Fu, Y. Zhao, D. Yang, C. Jiao, G. Sun, Q. Wang, D. He, *Nanoscale* **2021**, *13*, 2502.
[51] Z. Yang, Q. Xu, X. Wang, J. Lu, H. Wang, F. Li, L. Zhang, G. Hu, C. Pan, *Adv. Mater.* **2018**, *30*, 1802110.
[52] D. Shi, V. Adinolfi, R. Comin, M. Yuan, E. Alarousu, A. Buin, Y. Chen, S. Hoogland, A. Rothenberger, K. Katsiev, Y. Losovyj, X. Zhang, P. A. Dowben, O. F. Mohammed, E. H. Sargent, O. M. Bakr, *Science* **2015**, *347*, 519.
[53] P. Russo, M. Xiao, R. Liang, N. Y. Zhou, *Adv. Funct. Mater.* **2018**, *28*, 1706230.
[54] Y. Liu, Y. Wei, M. Liu, Y. Bai, G. Liu, X. Wang, S. Shang, W. Gao, C. Du, J. Chen, Y. Liu, *Angew. Chem., Int. Ed.* **2021**, *60*, 17440.
[55] J. Sun, S. Oh, Y. Choi, S. Seo, M. J. Oh, M. Lee, W. B. Lee, P. J. Yoo, J. H. Cho, J. H. Park, *Adv. Funct. Mater.* **2018**, *28*, 1804397.

© 2022 Wiley-VCH GmbH